

## Article

# Enhanced Performance of $\text{LiAl}_{0.1}\text{Mn}_{1.9}\text{O}_4$ Cathode for Li-Ion Battery via TiN Coating

Pinelopi Angelopoulou <sup>1,2</sup>, Spyros Kassavetis <sup>3</sup>, Joan Papavasiliou <sup>1,2</sup>, Dimitris Karfaridis <sup>3</sup>, Grzegorz Słowik <sup>4</sup>, Panos Patsalas <sup>3</sup> and George Avgouropoulos <sup>1,\*</sup>

<sup>1</sup> Department of Materials Science, University of Patras, GR-26504 Rio Patras, Greece; pangel@upatras.gr (P.A.); ipapavas@upatras.gr (J.P.)

<sup>2</sup> Foundation for Research and Technology-Hellas (FORTH), Institute of Chemical Engineering Sciences (ICE-HT), P.O. Box 1414, GR-26504 Patras, Greece

<sup>3</sup> Department of Physics, Aristotle University of Thessaloniki, GR-54124 Thessaloniki, Greece; skasa@physics.auth.gr (S.K.); dkarfari@physics.auth.gr (D.K.); ppats@physics.auth.gr (P.P.)

<sup>4</sup> Faculty of Chemistry, University of Maria Curie-Skłodowska, Pl. M. Curie-Skłodowskiej 2, 20-031 Lublin, Poland; grzegorz.slowik@poczta.umcs.lublin.pl

\* Correspondence: geoavg@upatras.gr

**Abstract:** The present work addresses the issues related to the capacity fading of spinel  $\text{LiMn}_2\text{O}_4$ , such as Mn leaching and Jahn–Teller distortion and suggests an advanced TiN-coated  $\text{LiAl}_{0.1}\text{Mn}_{1.9}\text{O}_4$  (LAMO) cathode material as an electrode for lithium-ion batteries. TiN coating layers with the same thickness but a different porosity cover the  $\text{LiAl}_{0.1}\text{Mn}_{1.9}\text{O}_4$  electrode via reactive magnetron sputtering, and present promising electrochemical behavior. In contrast with the pristine  $\text{LiAl}_{0.1}\text{Mn}_{1.9}\text{O}_4$ , the dense TiN-coated  $\text{LiAl}_{0.1}\text{Mn}_{1.9}\text{O}_4$  electrode demonstrates a remarkable long-term cycling by reducing the contact area of the electrode/electrolyte interface, resulting in structure stabilization.

**Keywords:** Li-ion batteries; LiMn spinel; cathode electrode; TiN coating



**Citation:** Angelopoulou, P.; Kassavetis, S.; Papavasiliou, J.; Karfaridis, D.; Słowik, G.; Patsalas, P.; Avgouropoulos, G. Enhanced Performance of  $\text{LiAl}_{0.1}\text{Mn}_{1.9}\text{O}_4$  Cathode for Li-Ion Battery via TiN Coating. *Energies* **2021**, *14*, 825. <https://doi.org/10.3390/en14040825>

Academic Editor:

Senentxu Lanceros-Mendez

Received: 4 January 2021

Accepted: 1 February 2021

Published: 4 February 2021

**Publisher's Note:** MDPI stays neutral with regard to jurisdictional claims in published maps and institutional affiliations.



**Copyright:** © 2021 by the authors. Licensee MDPI, Basel, Switzerland. This article is an open access article distributed under the terms and conditions of the Creative Commons Attribution (CC BY) license (<https://creativecommons.org/licenses/by/4.0/>).

## 1. Introduction

Favorable properties such as high energy density, a non-memory effect and a long lifetime [1,2] make lithium-ion batteries (LIBs) the most widely used energy storage mediums for a variety of portable power applications in everyday life. However, in order to compete with other rapidly growing technologies such as (hybrid) electric vehicles [3], there are still several issues to be solved, including the demand for higher power densities, enhanced cycle stability and safety. A great part of research worldwide is being directed to cathode development, which is the capacity-determining component in lithium-ion battery technology. From this perspective, lithium-ion cells utilizing spinel  $\text{LiMn}_2\text{O}_4$  cathodes with a theoretical capacity of  $148 \text{ mAh g}^{-1}$  are a good choice due to their high capacities, abundant source of manganese, low cost, low environmental impact and so on [4,5].

Despite the unique advantages, the application of  $\text{LiMn}_2\text{O}_4$  in commercial LIBs cannot be realized since this type of electrode experiences rapid capacity fading upon cycling. The spinel material undergoes degradation attributed to the Jahn–Teller effect and Mn leaching [4,5]. A synergistic effect of these two main factors (both related to the increased content of  $\text{Mn}^{3+}$  in cathodes, as discussed below), could affect the electrochemical behavior of the cell. The Jahn–Teller distortion of  $\text{Mn}^{3+}$  ions (with electronic configuration,  $t_{2g}^3 e_g^1$ ) is associated with structural instability, especially in the 3 V region [6]. Since the diffusion rate of lithium ions in electrolytes is faster than those inside  $\text{LiMn}_2\text{O}_4$  particles [7] at the end of discharge and especially at high current densities, lithium ions in a non-equilibrium dynamic condition accumulate at voltages  $>3 \text{ V}$  first at the spinel ( $\text{LiMn}_2\text{O}_4$ ) particle surface, transforming the electrode active material to  $\text{Li}_{1+x}\text{Mn}_2\text{O}_4$  [8,9]. The obtained  $\text{Mn}^{3+}$ -rich region causes a transformation of the crystal structure on the surface of  $\text{LiMn}_2\text{O}_4$  particles from cubic ( $c/a = 1$ ) to tetragonal ( $c/a = 1.16$ ) symmetry [8,10].

This can influence the three-dimensional pathways for Li ion diffusion, resulting in the capacity fading of active material [10]. In order to suppress the Jahn–Teller distortion and ensure the structural integrity of the electrode, many researchers have proposed replacing the small amount of trivalent manganese ions in the octahedral sites with several metal cations [11–13]. Following the same strategy, we recently studied combustion-synthesized  $\text{Li}_x\text{Mn}_2\text{O}_4$  nanostructures effectively doped with aluminium ions that minimized capacity fading and resulted in enhanced electrochemical performance, especially in comparison with undoped samples [14].

The second mechanism concerns the dissolution of  $\text{Mn}^{2+}$  in a liquid electrolyte as a result of the corrosive reaction between  $\text{LiMn}_2\text{O}_4$  and the electrolyte, according to J.C Hunter [15]:  $2\text{Mn}^{3+}_{(\text{solid})} \rightarrow \text{Mn}^{4+}_{(\text{solid})} + \text{Mn}^{2+}_{(\text{solution})}$ . This reaction dominates the end of the discharge as the concentration of  $\text{Mn}^{3+}$  species maximizes. After that, the  $\text{Mn}^{2+}$  species migrate towards the anode and are reduced to metallic manganese, thereby increasing the cell impedance and influencing the solid electrolyte interface (SEI) [16,17]. At the same time, the insoluble  $\text{Mn}^{4+}$  ions remain on the cathode surface, which leads to severe capacity fading since they do not participate in the electrochemical reaction. The aforementioned reaction is favored using  $\text{LiPF}_6$  as the electrolyte, as it reacts with water towards hydrofluoric acid [18,19]. Engineering the electrode's surface using various coating technologies is an effective way to block these undesired reactions by preventing direct contact between the electrolyte and  $\text{LiMn}_2\text{O}_4$  [20]. These coating materials include various oxides [21–27], active electrode materials [28–30], graphene [31], conductive polymers [32] and so on. Several coating technologies have been proposed to improve the integrity and uniformity of a coating layer with an uninterrupted protective layer/electrode interface and an optimum microstructure that can affect the transport of  $\text{Li}^+$  and  $\text{e}^-$ , especially at high performance rates. Current technologies include chemical methods such as sol-gel [33], coprecipitation [34] and chemical vapor deposition (CVD) [35], as well as physical methods such as atomic layer deposition (ALD) [36] and physical vapor deposition (PVD) [37].

Based on previous work where the successful Al doping of spinel  $\text{LiMn}_2\text{O}_4$  minimized capacity fading [14], we take a step forward in this study to report on the modification of the cathode surface  $\text{LiAl}_{0.1}\text{Mn}_{1.9}\text{O}_4$  with a titanium nitride (TiN) coating layer via magnetron sputtering. Magnetron sputtering is a functional technique in which thin films can easily be obtained by carefully controlling the desired porosity and thickness. TiN compound, which has previously been applied as a coating layer for an anode [38–40] and an  $\text{LiFePO}_4$  cathode [41] in LIBs, possesses excellent chemical resistance and mechanical and electrical properties [42]. Most importantly, its electrical conductivity is extremely high, ranging from 4000 to 55,500  $\text{S cm}^{-1}$  [43,44], depending on the crystalline quality of TiN, as well as its grain size and stoichiometry (overstoichiometric  $\text{TiN}_x$  ( $x > 1$ ) can be less conductive due to Ti vacancies that act as electron recombination sites [45]). To the best of our knowledge, titanium nitride has not previously been reported as a coating material for spinel  $\text{LiMn}_2\text{O}_4$ . Herein, we study TiN-coated  $\text{LiAl}_{0.1}\text{Mn}_{1.9}\text{O}_4$  electrodes with a common thickness but different coating material porosities. A pristine  $\text{LiAl}_{0.1}\text{Mn}_{1.9}\text{O}_4$  electrode is also examined for comparison.

## 2. Materials and Methods

### 2.1. Materials Synthesis

$\text{LiAl}_{0.1}\text{Mn}_{1.9}\text{O}_4$  spinel oxide was synthesized via the combustion method described previously [46] where lithium nitrate anhydrous ( $\text{LiNO}_3$ , 99%, Alfa Aesar, Kandel, Germany), manganese nitrate hydrate ( $\text{Mn}(\text{NO}_3)_2 \cdot \text{H}_2\text{O}$ ,  $x \sim 4\text{--}6$ , 98%, Aldrich, LSC, Athens, Greece) and aluminum nitrate ( $\text{Al}(\text{NO}_3)_3 \cdot 9\text{H}_2\text{O}$ , 98–102%, Alfa Aesar, Kandel, Germany) served as oxidizer and urea ( $\text{CO}(\text{NH}_2)_2$ , 99%, Aldrich, LSC, Athens, Greece) as fuel. The precursors were dissolved in deionized water and stirred at 200 °C, before being transferred in a muffle furnace preheated to 500 °C. The reaction took place immediately, yielding a foamy and voluminous powder. The as-prepared solids were then further calcined at 600 °C for 2 h. Details about the synthesis route have been reported in a previous work [14].

The cathode electrode was made as follows: a slurry containing  $\text{LiAl}_{0.1}\text{Mn}_{1.9}\text{O}_4$  active material (77.5 wt.%), conductive carbon (20 wt.%) and polymer binder PVdF (2.5 wt.%) in excess of dimethylformamide (DMF) was mixed for 1 h. The blended slurry was manually brush-coated on an Al foil current collector (square sheet of  $16\text{ cm}^2$ ) placed on a vacuum table and heated to  $100\text{ }^\circ\text{C}$ . The loading of the active material was  $1\text{ mg cm}^{-2}$ .

Titanium nitride (TiN) was deposited onto the surface of  $\text{LiAl}_{0.1}\text{Mn}_{1.9}\text{O}_4$  electrodes using reactive magnetron sputtering. For the sputter deposition, a high vacuum chamber ( $P_b < 5 \times 10^{-7}$  mbar) equipped with a 6" Ti (99.999% pure) DC cathode was implemented as described in [45]. The Ar and Nitrogen flows (both 99.999% purity) were 15 and 2.3 sccm, respectively, and the target power was 450 W-DC operating in metallic reactive sputter mode. The substrate to target distance was 65 mm. The entire growth took place without intentional heating, but a macroscopic temperature up to  $130\text{ }^\circ\text{C}$  was recorded due to the plasma and ion bombardment. Two biasing conditions were used. In the first, the substrates were floating (self-biasing  $-20\text{ V}$ ), resulting in underdense ( $4.3\text{ g/cm}^3$ ), porous, overstoichiometric ( $\text{TiN}_x > 1$ ) and less conductive films [45,47–52] prone to oxidation [53]. Secondly, when intentional biasing  $V_b = -120\text{ V}$  was applied, the films became fully dense ( $5.7\text{ g/cm}^3$ ), stoichiometric, highly conductive [45,47–52] and oxidation-resistant [53]. The nominal thickness of both films was determined to be 50 nm according to the deposition rates reported in [48,49]. The reproducibility of the growth with the reported past experiments [45,47–52] was checked by comparing the spectroscopic ellipsometry spectra of old and new reference samples grown on Si in the same run with the coating of the electrodes. The surface-modified electrodes that were encoded are hereafter labeled as TiN-LAMO\_50\_D and TiN-LAMO\_50\_P in reference to the dense 50 nm TiN layer and the porous layer, respectively, while the reference electrode is noted as bare LAMO.

## 2.2. Physicochemical Characterization

Experimental methods for the physicochemical characterization of the synthesized materials and surfaces are described in detail in our previous works [14,46]. Powder X-ray diffraction (XRD; Bruker D8 Advance, Bruker, Birmingham, UK; Cu Ka radiation at 40 kV and 40 mA) was employed to identify the crystal structure of the electrodes. A scanning electron microscope (SEM-EDS; ZEISS EVO MA 10; Carl Zeiss SMT AG Company, Oberkochen, Germany) and transmission electron microscope (TEM; FEI Titan G2 60–300; FEI, Gräfelfing, Germany) were used to investigate the morphology of electrodes. Wide scan and core-level X-ray photoelectron Spectra (XPS) were collected using a KRATOS Axis Ultra DLD system (Kratos Analytical Ltd., Manchester, United Kingdom; monochromated  $\text{AlK}_\alpha$  X-ray source; hemispherical sector electron analyzer; multichannel electron detector; 20 eV pass energy). A C-1s peak of contaminant carbon and an Ar-2p peak used for cleaning the surface after sputter etching were used to calculate the spectral shifts and binding energies. Spectra deconvolution was done via Shirley background subtraction, using Gaussian-Lorentzian product peaks (70% Gaussian, 30% Lorentzian).

## 2.3. Electrochemical Characterization

Conventional experimental procedures were applied as described previously [19,46] to evaluate the electrochemical behavior of the as-prepared electrodes at ambient conditions. Briefly, two-electrode Swagelok-type cells were assembled in an argon-filled glove box with a water concentration lower than 1 ppm, using lithium metal foil as a reference and counter electrodes and a porous inert polymer membrane (SCIMAT MG 38111; Scimt Ltd., Swindon, United Kingdom) as the separator. The electrolyte solution was composed of 1 M lithium hexafluorophosphate ( $\text{LiPF}_6$ ) in ethylene carbonate (EC)/dimethyl carbonate (DMC) (1:1 in volume). The cycling behavior of the cells was studied in a Basytec multichannel battery tester (BaSyTec GmbH, Asselfingen, Deutschland) applying a potential range of 3.0–4.8 V and a current rate of  $100\text{ mA g}^{-1}$  ( $1\text{ C} = 135.5\text{ mA g}^{-1}$  for  $\text{LiAl}_{0.1}\text{Mn}_{1.9}\text{O}_4$ ). Cyclic voltammetry measurements were carried out in a galvanostat/potentiostat apparatus (Autolab PGSTAT302N, Metrohm Autolab B.V., Utrecht, The Netherlands) using a scan rate

of  $1 \text{ mV s}^{-1}$  at 3.0–4.8 V. The electrochemical impedance spectroscopy (EIS) measurements were conducted at the same apparatus at a frequency range of  $10^5$ – $10^{-1}$  Hz, applying an AC amplitude of 10 mV. All potentials in this work refer to Li/Li<sup>+</sup>.

### 3. Results and Discussion

#### 3.1. Physicochemical Characterization

The structural modifications of LAMO electrodes were studied via XRD before and after surface coating. The diffraction peaks of all samples corresponded well to the cubic spinel structure with space group Fd3m (Figure S1; JCPDS card No. 35-0782) suggesting that the addition of TiN layers did not affect the basic crystal structure of LiMn<sub>2</sub>O<sub>4</sub>. Crystallite sizes of spinel-based active material were calculated from line broadening of the (111) peak via a Scherrer equation, and varied in the range of 23–29 nm (23 nm for the bare LAMO material). No reflections coming from titanium nitride phase could be observed in the X-ray diffractograms due to XRD detection limitations.

TEM images were collected for the modified electrodes in order to investigate their microstructures and verify the TiN layer covering the surface of the LiAl<sub>0.1</sub>Mn<sub>1.9</sub>O<sub>4</sub> spinel. As shown in Figure 1, crystalline TiN nanoparticles were present on the surface-modified electrodes. Lattice fringes of TiN (200), (220) and (111)—with their corresponding d-spacings of 0.212, 0.150 and 0.244 nm (JCPDS card No. 38-1420), respectively—can be observed clearly in the high-resolution TEM images. In some regions, the crystalline planes (111), (220), (311) and (511)—and their corresponding interplanar distances of 0.476, 0.291, 0.249 and 0.159 nm, respectively—can also be identified, and are attributable to the LiMn<sub>2</sub>O<sub>4</sub> spinel structure (JCPDS card No. 35-0782). EDS elemental mappings of selected regions of TiN-coated LiAl<sub>0.1</sub>Mn<sub>1.9</sub>O<sub>4</sub> electrodes (Figure 2) further confirm the uniform distribution of Mn, O, Al, Ti and N species, while carbon was derived from both conductive additive and graphite-coated substrate. These findings are further confirmed by XPS surface elemental analysis, as we will discuss below. The strength of the mapping trace depends on the different contents of various elements in LiAl<sub>0.1</sub>Mn<sub>1.9</sub>O<sub>4</sub> spinel particles [19].

The XPS wide scan spectra were used (Figure S2) to determine the surface elemental composition of the samples before and after electrochemical testing (Figure S3). In Figure S3a, XPS wide scan spectra indicate that the surfaces of all the studied samples (bare LAMO, TiN-LAMO\_50\_D and TiN-LAMO\_50\_P) were heavily contaminated by adventitious carbon and oxygen. It is worth noting that Mn was present in the samples even prior to electrochemical testing; we assigned it to pinholes existing in the films (i.e., the Mn originates from the substrate). The titanium nitride coated samples in Figure S3b exhibited Ti2s, Ti2p and N1s lines, suggesting the successful deposition of dense TiN and porous TiN<sub>x > 1</sub> [54,55] close to equiatomic compositions. The Ti2p<sub>3/2</sub> line is a sensitive probe of the oxidation state and stoichiometry of titanium in titanium nitride [56,57]. The Ti2p<sub>3/2</sub> spectra exhibited a fine structure that was attributable to the different phases and oxidation states of Ti in TiN and the relevant compounds indicated in Figure S3c. In particular, the lowest energy peak can be assigned to stoichiometric TiN [54,55], the peak at 456.3 eV to over-stoichiometric TiN<sub>x</sub> [58], the peak at 458 eV to TiO<sub>x</sub>N<sub>y</sub> [59] and, finally, the peak at 459.2 eV to TiO<sub>2</sub> [60].

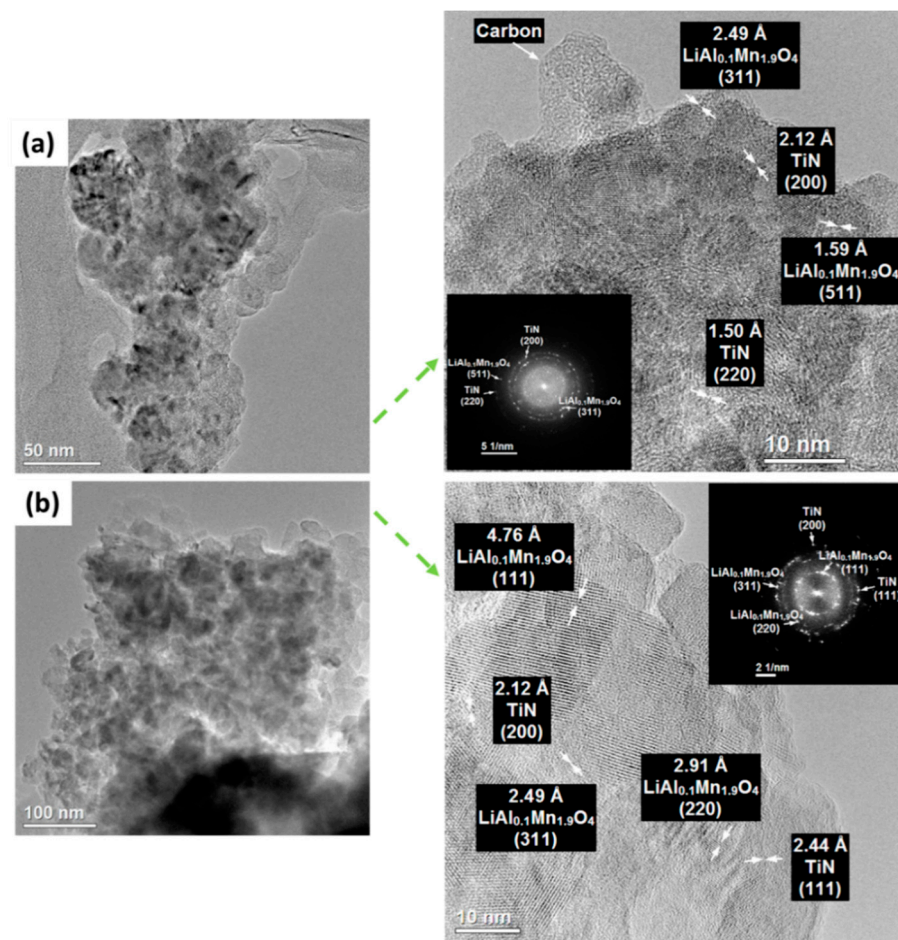


**Figure 1.** TEM images (on the left) and high resolution TEM (HRTEM) images with fast Fourier transforms (FFTs), (on the right) of (a) TiN-LAMO\_50\_D and (b) TiN-LAMO\_50\_P electrodes.

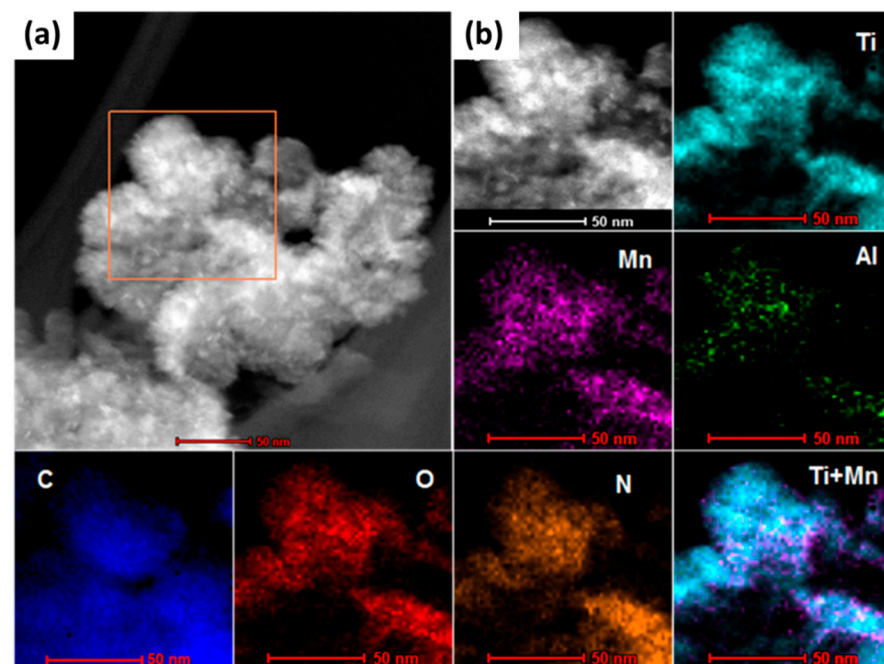


**Figure 2.** Cont.

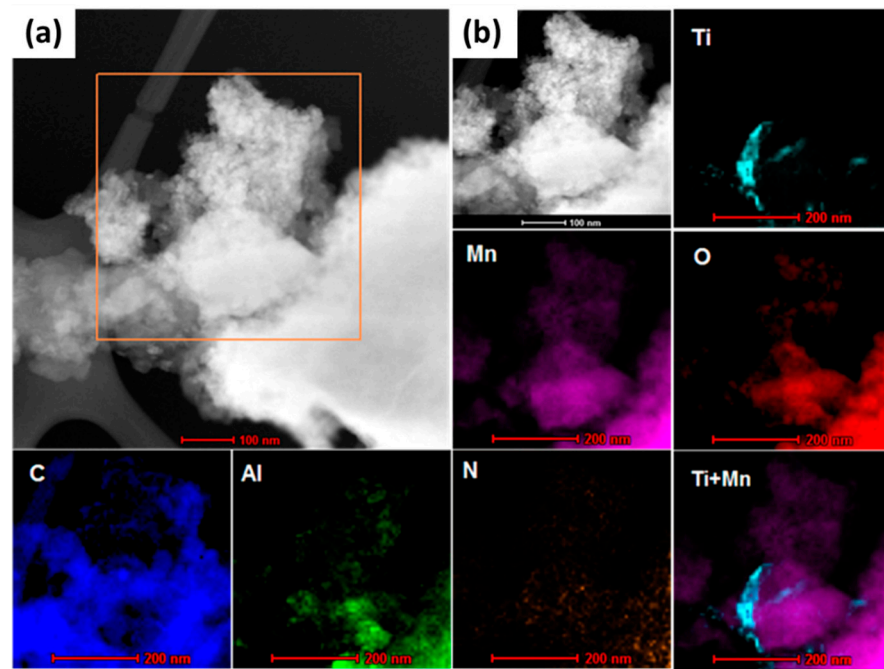


**Figure 2.** High-angle annular dark-field scanning transmission electron microscopy (HAADF-STEM) image of TiN-LAMO\_50\_D (upper) and TiN-LAMO\_50\_P (lower) electrode (a) and the corresponding energy dispersive X-ray spectroscopy (EDS) mapping results of the boxed region (b).

### 3.2. Electrochemical Characterization

The electrochemical characterization of the pristine and TiN-coated  $\text{LiAl}_{0.1}\text{Mn}_{1.9}\text{O}_4$  electrodes was carried out with galvanostatic charge-discharge measurements at room temperature. Figure 3a shows the cycling performance of the electrodes at  $100 \text{ mA g}^{-1}$  in the potential range of 3.0–4.8 V, while Figure S4 provides the Coulombic efficiency [61] of the cells during the first cycle. The bare LAMO, TiN-LAMO\_50\_D and TiN-LAMO\_50\_P electrodes exhibited initial discharge capacities of 109.8, 104.7 and 100.0  $\text{mAh g}^{-1}$ , respectively. However, after the long-term operation of 400 cycles, the surface-modified electrodes showed a remarkable stability compared to the bare LAMO. Indeed, the bare LAMO, TiN-LAMO\_50\_D and TiN-LAMO\_50\_P delivered 37.3, 76.3 and 60.7  $\text{mAh g}^{-1}$  (maintaining 34%, 72.9% and 60.7% capacity retention), respectively, after 400 cycles. It should be noted that the dense TiN layer affected the charge/discharge process in a more positive way, resulting in an enhanced cyclic stability compared to the porous layer. The charge-discharge profiles of the samples during the first and 400th cycle are shown in Figure 3b. As can clearly be seen, the bare electrode suffered from faster capacity fading due to degradation of the spinel nanoparticles (as demonstrated in the literature). The charge-discharge plateaus related to the lithium-ion insertion/extraction stage completely disappeared after 400 cycles in contrast with the covered electrodes, confirming the protective role of titanium nitride deposition in active material stabilization. Figure 3c displays the rate behavior of the bare LAMO and TiN-LAMO\_50\_D for current densities ranging from 200 to  $800 \text{ mA g}^{-1}$  in the potential window of 3.0–4.8 V. The coated electrode behaved with superiority to the pristine electrode when cycled under the same current rate. Interestingly, the bare sample provided almost 75  $\text{mAh g}^{-1}$  when the rate returned to  $200 \text{ mA g}^{-1}$ , while the surface-modified electrode delivered the same capacity for the double current rate. The Coulombic efficiency of TiN-LAMO\_50\_D was almost 100% for 250 cycles at different current rates, in addition to a significantly enhanced rate performance. The promoted performance of the modified electrode can be ascribed to (i) increased conductivity, which promoted a faster electron transport between the  $\text{LiAl}_{0.1}\text{Mn}_{1.9}\text{O}_4$  particles, and (ii) protection against manganese dissolution. Both of these achievements resulted from the TiN coating layer.

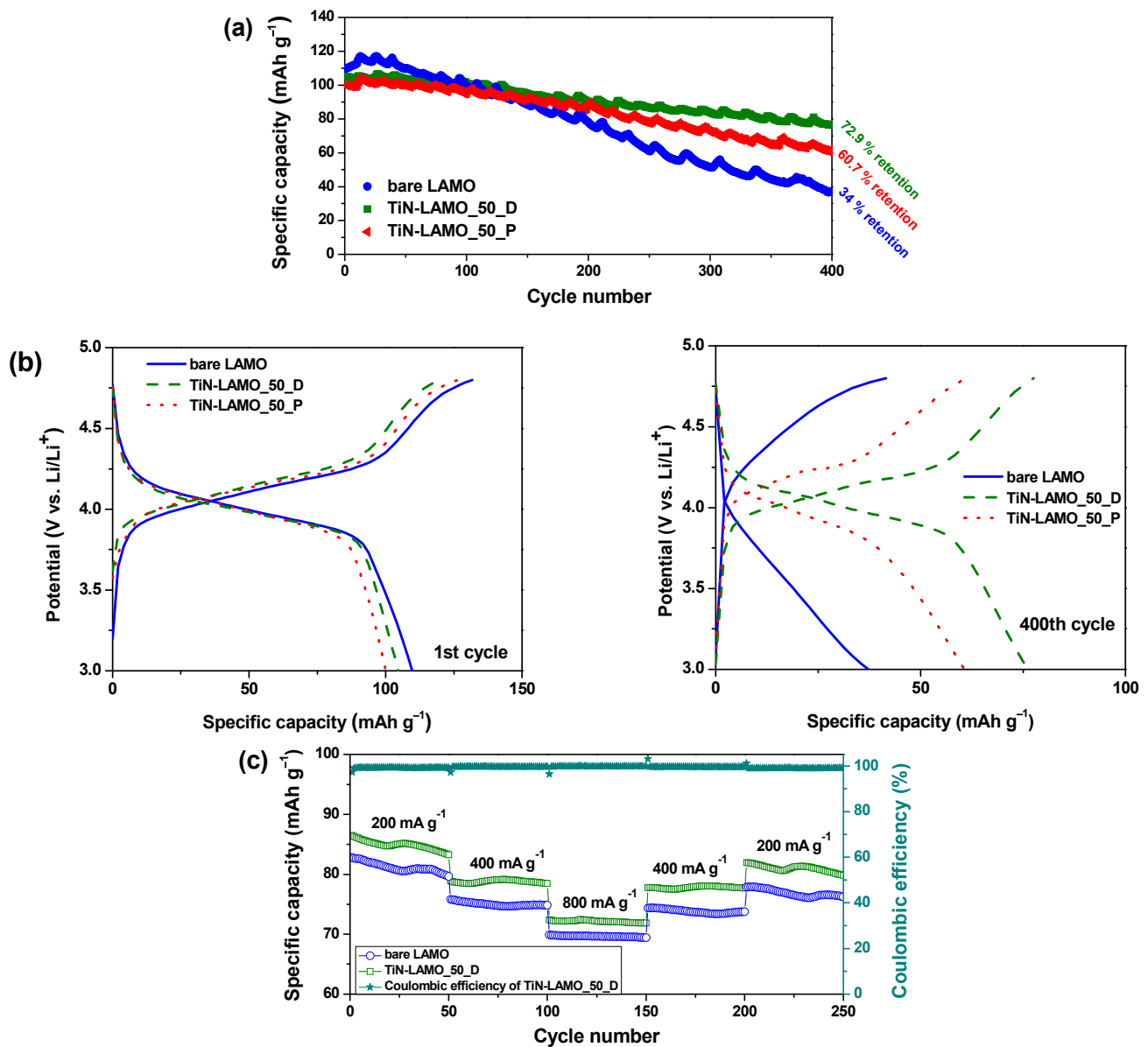


**Figure 3.** (a) Discharge capacities vs. cycle number, (b) charge-discharge profiles of the electrodes cycled at 100 mA g<sup>-1</sup> and (c) rate performance of bare LAMO and TiN-LAMO\_50\_D electrode, cycled at different current rates within a potential range of 3.0–4.8 V.

To obtain more insight into the active electrochemical surface area of the bare and surface-coated LiAl<sub>0.1</sub>Mn<sub>1.9</sub>O<sub>4</sub> electrodes, cyclic voltammograms were collected in the potential range of 3.0–4.8 V. Generally, LiMn<sub>2</sub>O<sub>4</sub> spinel materials show double oxidation and reduction peaks, which reflect the stepwise process of lithium ion insertion/extraction into the spinel structure [19,46,62]. Figure 4 displays the CV curves during various cycles. Apparently, the overlapping of the two characteristic peaks associated with Li ion insertion/extraction is related to limited lithium-ion diffusion at elevated scan rates [46]. Among the samples tested, TiN-LAMO\_50\_D showed the highest electrochemical surface area, as obtained from the various peaks. It is believed that the improved conductivity of an electrode with a dense TiN coating of 50 nm could allow for faster electrochemical reaction kinetics. Both types of peak decreased faster in the unmodified electrode, as compared with the rest of the samples. This is strong evidence of spinel protection and the improved reversibility of surface-coated electrodes. Moreover, the peak positions of the pristine LiAl<sub>0.1</sub>Mn<sub>1.9</sub>O<sub>4</sub> electrode were significantly shifted as cycling continued. Conse-

quently, higher oxidation and lower reduction potentials indicate the potential for a higher polarization of a bare  $\text{LiAl}_{0.1}\text{Mn}_{1.9}\text{O}_4$  electrode, which was induced by the lower electronic conductivity of this sample [19,46]. These findings reveal that spinel structures were more stable during the charge/discharge process and suppression of Mn dissolution in the surface-modified electrodes, which could partly explain the enhanced cycling stability.

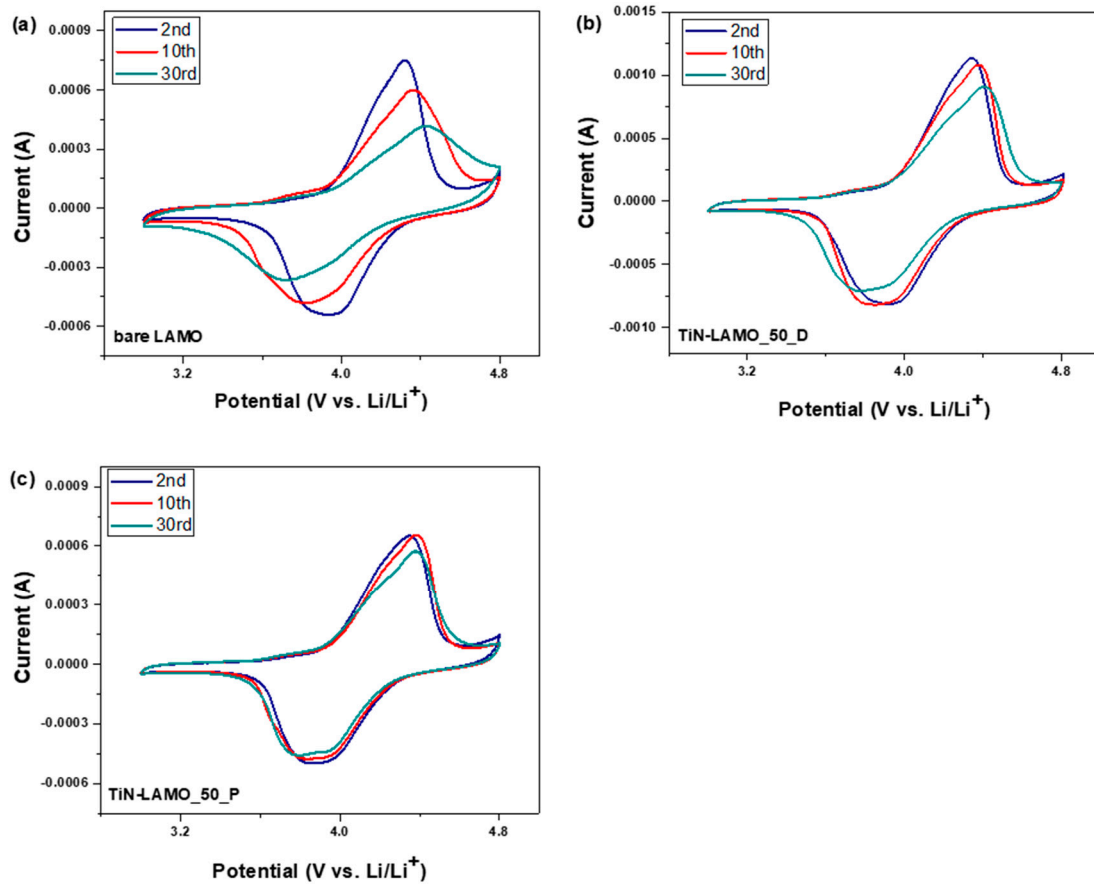


**Figure 4.** Cyclic voltammograms of (a) bare LAMO, (b) TiN-LAMO\_50\_D and (c) TiN-LAMO\_50\_P electrodes (scan rate:  $1 \text{ mV s}^{-1}$ ).

EIS measurements were recorded for all the samples in order to shed light into the processes taking place in bare and modified electrodes at a discharged state (3.0 V) cycled under a  $100 \text{ mA g}^{-1}$  current rate. Nyquist plots of the electrodes after 200 and 400 cycles are shown in Figure 5, along with the equivalent circuit used to simulate the experimental data. The values of the fitted resistance parameters are listed in Table S1, and the corresponding fitting curves are presented in Figure S5. After prolonged cycling (from the 200th to 400th cycle), the measured impedances  $R_f$  and  $R_{ct}$  show an increasing trend for all the samples that resulted from the extended surface passivation and degradation of spinel particles. Table S1 shows that the increase of  $R_f$  from the 200th to 400th cycle was significantly lessened in the surface-modified electrodes with the following trend  $\text{TiN-LAMO}_50\text{D} < \text{TiN-LAMO}_50\text{P}$ , as compared to the bare one. The film resistances defined the long-term operation of electrodes, since the lower values of  $R_f$  led to enhanced capacity retention and, ultimately, the protective layer suppressed the formation of the passivation layer on the electrode surface. After the 400th discharge, the TiN-LAMO\_50\_D electrode exhibited the smallest  $R_{ct}$  ( $31.5 \Omega$ ) among the other samples, indicating a facile  $\text{Li}^+$  transport due to the effective surface stabilization from the dense 50 nm protective layer.

The lithium-ion diffusion coefficient  $D_{\text{Li}^+}$  can be calculated by the following equations [63]:

$$Z' = R_f + R_{ct} + \sigma\omega^{-0.5} \quad (1)$$

$$D_{\text{Li}^+} = \frac{R^2 T^2}{2A^2 n^4 F^4 C_{\text{Li}}^2 \sigma^2} \quad (2)$$

where  $Z'$ ,  $\omega$ ,  $R$ ,  $T$ ,  $A$ ,  $n$ ,  $F$  and  $C$  refer to the real part of the impedance, the angular frequency in the low-frequency region, the gas constant, the absolute temperature, the contact surface area between electrode and electrolyte, the number of reaction electrons per molecule during oxidization, the Faraday constant and the molar  $\text{Li}^+$  concentration in the electrolyte, respectively. Moreover,  $\sigma$  represents the Warburg factor, which is relative to  $Z'$  (Equation (1) and can be obtained from the slope of the linear relationship between  $Z'$  and  $\omega^{-0.5}$  in the low-frequency region (Figure 6)). The calculated lithium-ion coefficient values of the bare LAMO, TiN-LAMO\_50\_D and TiN-LAMO\_50\_P after 400 cycles were  $5.24 \times 10^{-14}$ ,  $1.79 \times 10^{-13}$  and  $1.25 \times 10^{-13} \text{ cm}^2 \text{ s}^{-1}$ , respectively. The TiN-LAMO\_50\_D electrode possessed the highest  $D_{\text{Li}^+}$ , indicating an enhanced  $\text{Li}^+$  transfer believed to be a consequence of the stabilized surface and structure provided by the TiN coating.

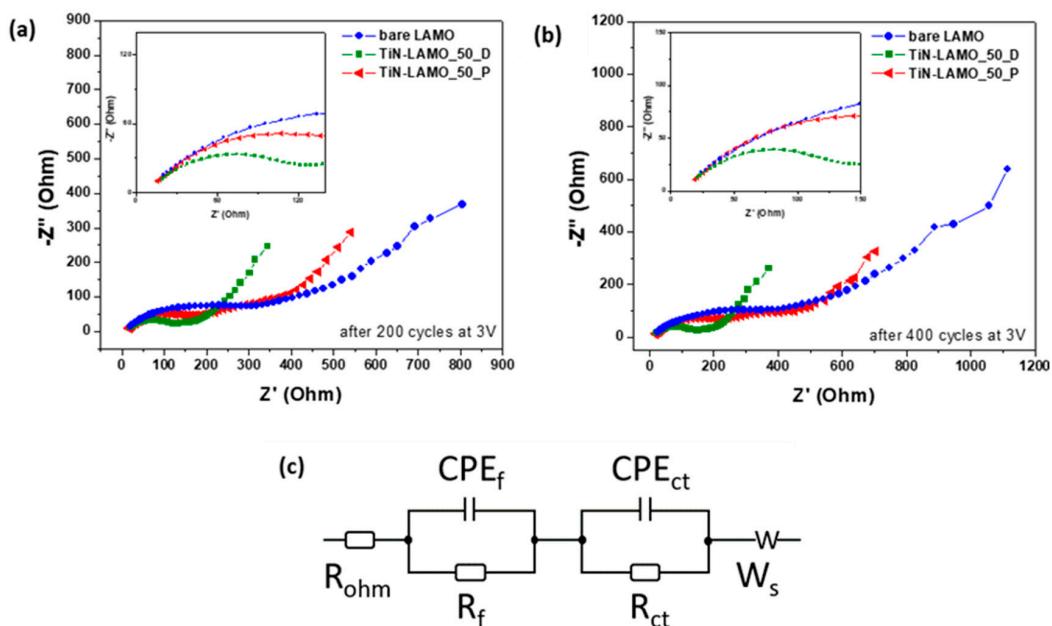


**Figure 5.** Nyquist plots of the electrodes at a discharged state of 3.0 V after (a) 200 cycles and (b) 400 cycles, and (c) the equivalent circuit that describes the experimental data.  $R_{\text{ohm}}$ : ohmic resistance of the cell;  $R_f$ : interfacial film resistance;  $R_{\text{ct}}$ :  $\text{Li}^+$  charge transfer resistance at the electrode-electrolyte interface;  $CPE_f$ : capacitance of the electrical double layer;  $CPE_{\text{ct}}$ : “imperfect” double-layer capacitor;  $CPE_{\text{ct}}$ : capacitance of the double layer;  $W_s$ : the Warburg impedance corresponding to the low-frequency tail (the  $\text{Li}^+$  diffusion in the spinel structure).

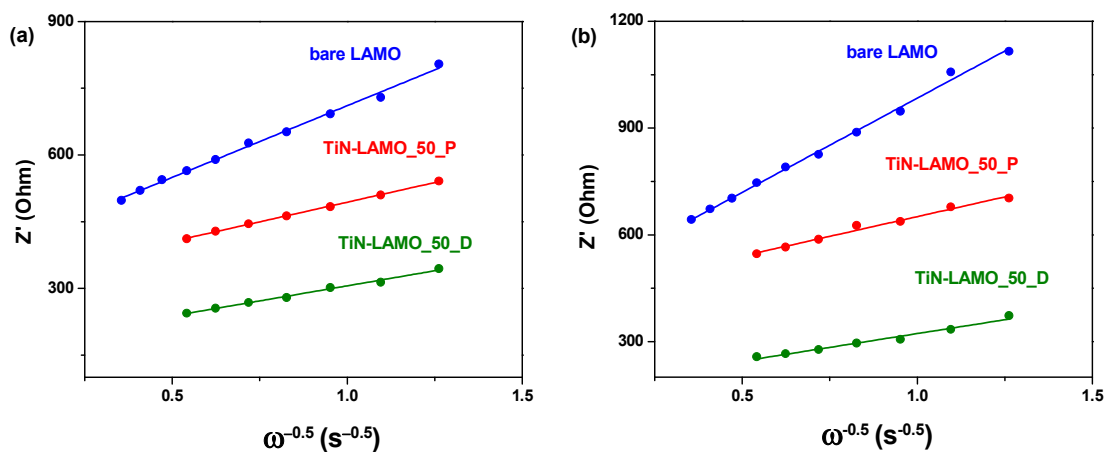


**Figure 6.** The relationship between  $Z'$  and  $\omega^{-0.5}$  for the electrodes (a) after 200 cycles and (b) after 400 cycles.

### 3.3. EDS/XPS Analysis after Cycling

Post-mortem analysis of the cycled TiN-LAMO\_50\_D electrode via SEM/EDS (Figure S6) revealed that this electrode contained more manganese as compared to the uncoated  $\text{LiAl}_{0.1}\text{Mn}_{1.9}\text{O}_4$  electrode, demonstrating the strong shielding effect of titanium nitride deposition against manganese dissolution in the electrolyte, which clearly explains the large difference of capacity retention observed in Figure 3a.

XPS after electrochemical testing suggested that all surfaces were enriched with F (Figure S3). The TiN-LAMO\_50\_D sample successfully endured electrochemical testing, and Ti and N were still present in the wide scan spectra (in Figure S2) along with the  $\text{Ti}2p_{3/2}$  core levels (in Figure S3c) that resulted from significant contribution to the surface composition, according to Figure S3a. On the contrary, the TiN-LAMO\_50\_P sample showed a substantial removal of Ti from the surface to the verge of elimination, both in the wide scan spectra (Figure S2) and the  $\text{Ti}2p_{3/2}$  core levels and total oxidation of any Ti-remnants to form  $\text{TiO}_2$  (Figure S3). The  $\text{Mn}2p_{3/2}$  core level (Figure 7) spectra provide further relevant insights. The LAMO sample exhibited an exclusive peak of  $\text{Mn}2p_{3/2}$  with an energy-binding characteristic in the spinel  $\text{LiMn}_2\text{O}_4$  (Figure 7) [64]. After electrochemical testing, there was a strong evidence for the existence of  $\text{MnO}_2$  [65] on the surface of the LAMO, and a potential indication of the formation of  $\text{MnO}$  via the existence of a characteristic satellite peak at 646 eV [65]. It has to be noted that this peak was accompanied by a dominant satellite peak of  $\text{MnO}$  at around 641 eV [66]. Thus, the  $\text{Mn}2p_{3/2}$  core levels were deconvoluted to contributions of Mn for valence II, III, IV, VI and VII (note that the valence VII peak overlaps with the satellite of valence II) according to [66], as shown in Figure 7a; the results of the deconvolution are summarized in Figure 7b. Before cycling, the Mn in the TiN-LAMO\_50\_D and  $\text{LiAl}_{0.1}\text{Mn}_{1.9}\text{O}_4$  samples was mostly present in valence IV ( $\text{MnO}_2$ ), while it decreased in the dense electrode and remained intact in bare LAMO after the electrochemical testing. On the contrary, the Mn in the TiN-LAMO\_50\_P sample was mostly present in valence III, suggesting that the deposition of  $\text{TiN}_x$  promoted surface defects on the  $\text{LiAl}_{0.1}\text{Mn}_{1.9}\text{O}_4$  substrate. Moreover, before electrochemical testing,  $\text{Mn}^{2+}$  could be observed in the TiN-LAMO\_50\_D, despite the fact that only valences III and IV were supposed to be detected in fresh spinel material. The lower average oxidation state might be associated with the minimal removal of oxygen atoms from spinel material during the sputtering process. This could be more intense in the case of a dense coating layer, depending on the different deposition conditions of the two samples, as previously discussed. After electrochemical testing, the LAMO sample did not show any significant valence difference, while the Mn in TiN-LAMO\_50\_D switched mostly to valence III (from valence IV). On the contrary, TiN-LAMO\_50\_P switched from valence III to valences IV and VI, which resemble the bare  $\text{LiAl}_{0.1}\text{Mn}_{1.9}\text{O}_4$  sample, and thus this might have been the result of the removal of  $\text{TiN}_x$  from the  $\text{LiAl}_{0.1}\text{Mn}_{1.9}\text{O}_4$  surface, exposing the underlying  $\text{LiAl}_{0.1}\text{Mn}_{1.9}\text{O}_4$  itself. It is evident that the TiN-LAMO\_50\_D sample was superior to the TiN-LAMO\_50\_P in terms of its durability in the electrochemical test, which is in accordance with its high density ( $5.7 \text{ g/cm}^3$ ) [46] and hardness (24.5 GPa) [47].

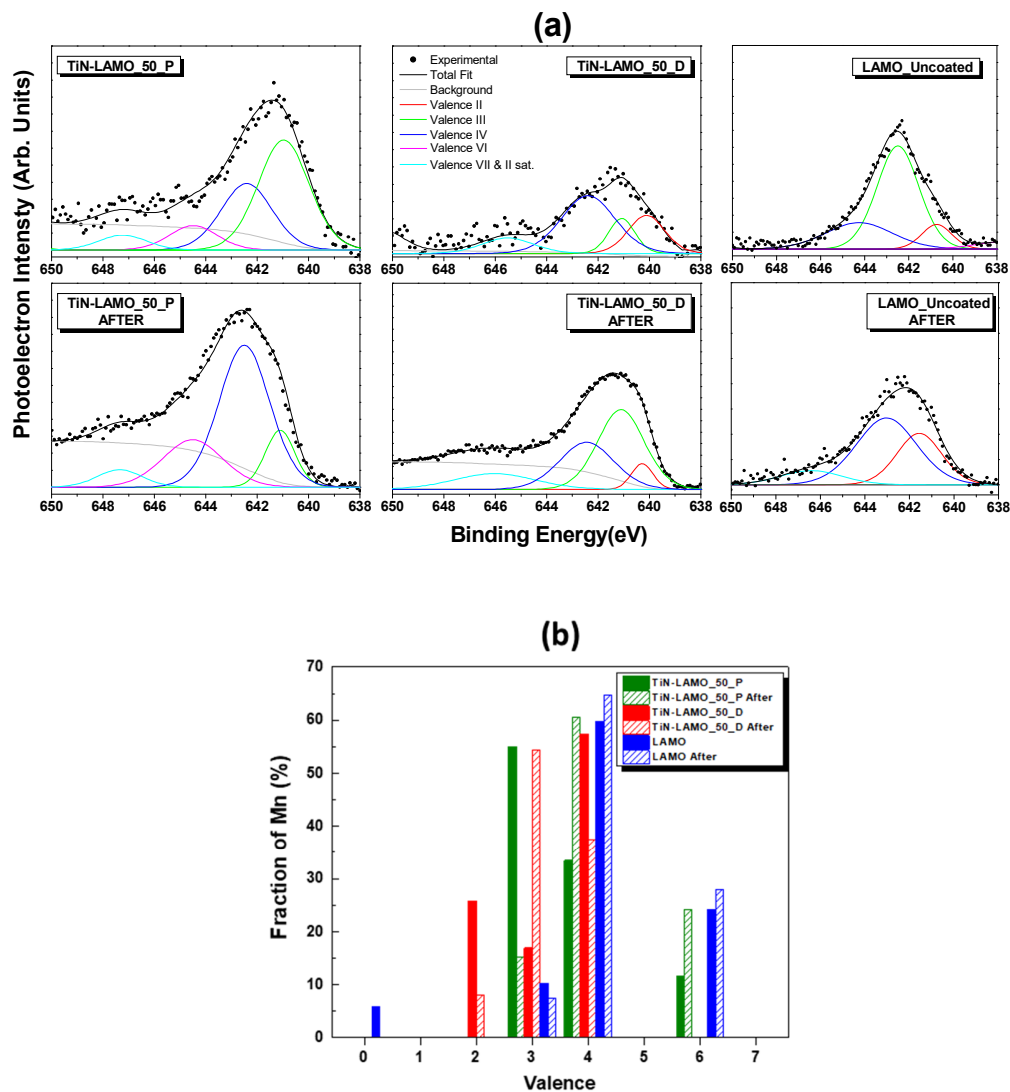


**Figure 7.** (a) Mn<sub>2p<sub>3/2</sub></sub> core level spectra of the studied samples before (top panels) and after (bottom panels) electrochemical testing for the studied samples deconvoluted into the contributions of the various Mn valences according to [66]. (b) Quantitative results of the deconvolution before and after electrochemical testing.

#### 4. Conclusions

Titanium nitride coatings of the same thickness but with different porosities deposited onto the surface of LiAl<sub>0.1</sub>Mn<sub>1.9</sub>O<sub>4</sub> electrodes proved capable of enhancing the cathode performance in a LIB cell by protecting and stabilizing the spinel material. The dense TiN-coated electrode was the most beneficial approach, leading to superior capacity retention, while the uncovered electrode showed severe capacity fading, implying faster spinel degradation. The effectiveness of the dense TiN layer compared to the porous one is estimated to have resulted from the better metallic behavior of the former, promoting the electron transport to the inner active material and thus allowing for faster electrochemical reaction kinetics. CV measurements confirmed the improved reversibility for surface-coated electrodes while EIS data accompanied with the calculated lithium-ion coefficient values revealed the enhanced Li<sup>+</sup> transport promoted by the protective layer. XPS confirmed the removal of the porous TiN<sub>x</sub> layer from the LiAl<sub>0.1</sub>Mn<sub>1.9</sub>O<sub>4</sub> surface, while the dense TiN layer remained intact after the electrochemical measurements. In the latter case, a slight removal of oxygen atoms from the spinel framework during the TiN sputtering process cannot be excluded, as indicated by the existence of Mn<sup>2+</sup> before the electrochemical testing. As for the bare LiAl<sub>0.1</sub>Mn<sub>1.9</sub>O<sub>4</sub> electrode after the long-term

operation, there is strong evidence of the existence of  $\text{MnO}_2$  and a potential indication of the formation of  $\text{MnO}$ , implying a cause of disproportional reaction where  $\text{Mn}^{4+}$  ions remain on the cathode surface and lead to severe capacity fading. This research enables the design of new cathode electrodes utilizing protective layers against side reactions, showing promising behavior for next-generation LIBs.

**Supplementary Materials:** The following are available online at <https://www.mdpi.com/1996-1073/14/4/825/s1>, Figure S1: XRD patterns of the bare LAMO, TiN-LAMO\_50\_D and TiN-LAMO\_50\_P electrodes. Figure S2: XPS wide scan spectra for bare LAMO, TiN-LAMO\_50\_D and TiN-LAMO\_50\_P before (upper panel) and after (lower panel) electrochemical testing. Figure S3: (a) The surface elemental composition of the studied samples before and after electrochemical testing, as extracted from XPS wide scan spectra taking into account the corresponding sensitivity factors and (b) the ratios of the  $[\text{N}]/[\text{Ti}]$  and  $[\text{O}]/[\text{Mn}]$  surface compositions showing that the as grown samples are almost equiatomic TiN and LAMO with O-rich surfaces, (c)  $\text{Ti}2p_{3/2}$  core level spectra of the two TiN-coated samples before and after electrochemical testing. The reference lines (based on Ref. 53–54,57–59) of various Ti-based phases are indicated by coloured vertical lines. Figure S4: Coulombic efficiency of bare LAMO, TiN-LAMO\_50\_D and TiN-LAMO\_50\_P during cycling. Figure S5: EIS fitting curves of the (a) bare LAMO, (b) TiN-LAMO\_50\_D and (c) TiN-LAMO\_50\_P electrodes after 200 and 400 cycles. Figure S6: EDS analysis of the inset SEM image of (a) bare LAMO and (b) TiN-LAMO\_50\_D electrode, after long-term operation of 400 cycles. Table S1: Fit results of EIS for the cathode electrodes after the 200th and 400th discharge step at 3.0 V.

**Author Contributions:** Supervision, Conceptualization and Writing—Review & Editing, G.A.; Methodology, Investigation and Writing—Original Draft Preparation, P.A.; Formal Analysis, P.P.; Investigation, J.P.; G.S.; S.K.; D.K. All authors have read and agreed to the published version of the manuscript.

**Funding:** The authors are thankful to the General Secretariat for Research and Technology (GSRT) and Hellenic Foundation for Research & Innovation (HFRI) for financial support to carry out this work.

**Institutional Review Board Statement:** Not applicable.

**Informed Consent Statement:** Not applicable.

**Data Availability Statement:** Not applicable.

**Conflicts of Interest:** The authors declare no conflict of interest.

## References

1. Tarascon, J.M.; Armand, M. Issues and challenges facing rechargeable lithium batteries. *Nature* **2001**, *414*, 359–367. [[CrossRef](#)]
2. Liu, W.; Wang, M.; Long Gao, X.; Zhang, W.; Chen, J.; Zhou, H.; Zhang, X. Improvement of the high-temperature, high-voltage cycling performance of  $\text{LiNi}_{0.5}\text{Co}_{0.2}\text{Mn}_{0.3}\text{O}_2$  cathode with  $\text{TiO}_2$  coating. *J. Alloy. Compd.* **2012**, *543*, 181–188. [[CrossRef](#)]
3. Zeng, X.; Li, M.; El-Hady, D.A.; Alshitari, W.; Al-Bogami, A.S.; Lu, J.; Amine, K. Commercialization of Lithium Battery Technologies for Electric Vehicles. *Adv. Energy Mater.* **2019**, *9*, 1900161. [[CrossRef](#)]
4. Jang, D.H.; Shin, Y.J.; Oh, S.M. Dissolution of Spinel Oxides and Capacity Losses in 4 V Li /  $\text{Li}_x\text{Mn}_2\text{O}_4$  Cells. *J. Electrochem. Soc.* **1996**, *143*, 2204–2211. [[CrossRef](#)]
5. Wang, Y.; Cao, G. Developments in Nanostructured Cathode Materials for High-Performance Lithium-Ion Batteries. *Adv. Mater.* **2008**, *20*, 2251–2269. [[CrossRef](#)]
6. Yi, T.; Zhu, Y.; Zhu, R.; Zhou, L.; Li, P.; Shu, J. Physicochemical properties of  $\text{LiAl}_x\text{Mn}_{2-x}\text{O}_4$  and  $\text{LiAl}_{0.05}\text{Mn}_{1.95}\text{O}_{4-y}\text{F}_y$  cathode material by the citric acid-assisted sol–gel method. *Ionics* **2009**, *15*, 177–182. [[CrossRef](#)]
7. Das, S.R.; Majumder, S.B.; Katiyar, R.S. Kinetic analysis of the  $\text{Li}^+$  ion intercalation behavior of solution derived nano-crystalline lithium manganate thin films. *J. Power Sources* **2005**, *139*, 261–268. [[CrossRef](#)]
8. Gummow, R.J.; de Kock, A.; Thackeray, M.M. Improved capacity retention in rechargeable 4 V lithium/lithium-manganese oxide (spinel) cells. *Solid State Ion.* **1994**, *69*, 59–67. [[CrossRef](#)]
9. Park, O.K.; Cho, Y.; Yoo, H.C.; Song, H.K.; Cho, J. Who will drive electric vehicles, olivine or spinel? *Energy Environ. Sci.* **2011**, *4*, 1621–1633. [[CrossRef](#)]
10. Lucas, P.; Angell, C.A. Synthesis and Diagnostic Electrochemistry of Nanocrystalline  $\text{Li}_{1+x}\text{Mn}_{2-x}\text{O}_4$  Powders of Controlled Li Content. *J. Electrochem. Soc.* **2000**, *147*, 4459–4463. [[CrossRef](#)]
11. Yang, Z.; Wang, Y.; Chen, X.; Wu, H.; Zhang, Y.  $\text{Mg}^{2+}$  and  $\text{Ti}^{4+}$  Co-Doped Spinel  $\text{LiMn}_2\text{O}_4$  as Lithium-Ion Battery Cathode. *ChemistrySelect* **2019**, *4*, 9583–9589. [[CrossRef](#)]

12. Sakunthala, A.; Reddy, M.V.; Selvasekarapandian, S.; Chowdari, B.V.R.; Selvin, P.C. Synthesis of compounds,  $\text{Li}(\text{MMn}_{11/6})\text{O}_4$  ( $\text{M} = \text{Mn}_{1/6}, \text{Co}_{1/6}, (\text{Co}_{1/12}\text{Cr}_{1/12}), (\text{Co}_{1/12}\text{Al}_{1/12}), (\text{Cr}_{1/12}\text{Al}_{1/12})$ ) by polymer precursor method and its electrochemical performance for lithium-ion batteries. *Electrochim. Acta* **2010**, *55*, 4441–4450. [[CrossRef](#)]
13. Amaral, F.A.; Bocchi, N.; Brocenschi, R.F.; Biaggio, S.R.; Rocha-Filho, R.C. Structural and electrochemical properties of the doped spinels  $\text{Li}_{1.05}\text{M}_{0.02}\text{Mn}_{1.98}\text{O}_{3.98}\text{N}_{0.02}$  ( $\text{M} = \text{Ga}^{3+}, \text{Al}^{3+}, \text{or Co}^{3+}$ ;  $\text{N} = \text{S}^{2-} \text{ or } \text{F}^{-}$ ) for use as cathode material in lithium batteries. *J. Power Sources* **2010**, *195*, 3293–3299. [[CrossRef](#)]
14. Angelopoulou, P.; Paloukis, F.; Slowik, G.; Wójcik, G.; Avgouropoulos, G. Combustion-synthesized  $\text{Li}_x\text{Mn}_2\text{O}_4$ -based spinel nanorods as cathode materials for lithium-ion batteries. *Chem. Eng. J.* **2017**, *311*, 191–202. [[CrossRef](#)]
15. Hunter, J.C. Preparation of a new crystal form of manganese dioxide:  $\lambda\text{-MnO}_2$ . *J. Solid State Chem.* **1981**, *39*, 142–147. [[CrossRef](#)]
16. Tsunekawa, H.; Tanimoto, S.; Marubayashi, R.; Fujita, M.; Kifune, K.; Sano, M. Capacity fading of graphite electrodes due to the deposition of manganese ions on them in Li-ion batteries. *J. Electrochem. Soc.* **2002**, *149*, A1326–A1331. [[CrossRef](#)]
17. Amine, K.; Liu, J.; Kang, S.; Belharouak, I.; Hyung, Y.; Vissers, D.; Henriksen, G. Improved lithium manganese oxide spinel/graphite Li-ion cells for high-power applications. *J. Power Sources* **2004**, *129*, 14–19. [[CrossRef](#)]
18. Benedek, R.; Thackeray, M.M. Reaction energy for  $\text{LiMn}_2\text{O}_4$  spinel dissolution in acid. *Electrochem. Solid State Lett.* **2006**, *9*, A265–A267. [[CrossRef](#)]
19. Myung, S.T.; Amine, K.; Sun, Y.K. Surface modification of cathode materials from nano-to microscale for rechargeable lithium-ion batteries. *J. Mater. Chem.* **2010**, *20*, 7074–7095. [[CrossRef](#)]
20. Kalluri, S.; Yoon, M.; Jo, M.; Liu, H.K.; Dou, S.X.; Cho, J.; Guo, Z. Feasibility of Cathode Surface Coating Technology for High-Energy Lithium-ion and Beyond-Lithium-ion Batteries. *Adv. Mater.* **2017**, *29*, 1605807. [[CrossRef](#)]
21. Cho, J.; Kim, T.-J.; Kim, Y.J. Complete blocking of  $\text{Mn}^{3+}$  ion dissolution from a  $\text{LiMn}_2\text{O}_4$  spinel intercalation compound by  $\text{Co}_3\text{O}_4$  coating. *Chem. Commun.* **2001**, *12*, 1074–1075. [[CrossRef](#)]
22. Gnanaraj, J.S.; Pol, V.G.; Gedanken, A.; Aurbach, D. Improving the high-temperature performance of  $\text{LiMn}_2\text{O}_4$  spinel electrodes by coating the active mass with  $\text{MgO}$  via a sonochemical method. *Electrochem. Commun.* **2003**, *5*, 940–945. [[CrossRef](#)]
23. Lin, Y.M.; Wu, H.C.; Yen, Y.C.; Guo, Z.Z.; Yang, M.H.; Chen, H.M.; Sheu, H.S.; Wu, N.L. Enhanced high-rate cycling stability of  $\text{LiMn}_2\text{O}_4$  cathode by  $\text{ZrO}_2$  coating for Li-ion battery. *J. Electrochem. Soc.* **2005**, *152*, A1526–A1532. [[CrossRef](#)]
24. Lim, S.; Cho, J. PVP-functionalized nanometre scale metal oxide coatings for cathode materials: Successful application to  $\text{LiMn}_2\text{O}_4$  spinel nanoparticles. *Chem. Commun.* **2008**, *37*, 4472–4474. [[CrossRef](#)]
25. Wang, L.; Zhao, J.; Guo, S.; He, X.; Jiang, C.; Wan, C. Investigation of  $\text{SnO}_2$ -modified  $\text{LiMn}_2\text{O}_4$  Composite as Cathode Material for Lithium-ion Batteries. *Int. J. Electrochem. Sci.* **2010**, *5*, 1113–1126.
26. Guan, D.; Jeevarajan, J.A.; Wang, Y. Enhanced cycleability of  $\text{LiMn}_2\text{O}_4$  cathodes by atomic layer deposition of nanosized-thin  $\text{Al}_2\text{O}_3$  coatings. *Nanoscale* **2011**, *3*, 1465–1469. [[CrossRef](#)]
27. Kim, C.S.; Kim, K.; Yic, C.W. Characteristics and electrochemical performance of the  $\text{LiMn}_2\text{O}_4$  with  $\text{TiO}_2$  surface layer in lithium secondary batteries. *J. Ceram. Process. Res.* **2015**, *16*, 232–236.
28. Park, S.C.; Kim, Y.M.; Han, S.C.; Ahn, S.; Ku, C.H.; Lee, J.Y. The elevated temperature performance of  $\text{LiMn}_2\text{O}_4$  coated with  $\text{LiNi}_{1-x}\text{Co}_x\text{O}_2$  ( $x = 0.2$  and  $1$ ). *J. Power Sources* **2002**, *107*, 42–47. [[CrossRef](#)]
29. Liu, D.Q.; Liu, X.Q.; He, Z.Z. The elevated temperature performance of  $\text{LiMn}_2\text{O}_4$  coated with  $\text{Li}_4\text{Ti}_5\text{O}_{12}$  for lithium ion battery. *Mater. Chem. Phys.* **2007**, *105*, 362–366. [[CrossRef](#)]
30. Li, X.; Xu, Y. Enhanced cycling performance of spinel  $\text{LiMn}_2\text{O}_4$  coated with  $\text{ZnMn}_2\text{O}_4$  shell. *J. Solid State Electrochem.* **2008**, *12*, 851–855. [[CrossRef](#)]
31. Jaber-Ansari, L.; Puntambekar, K.P.; Kim, S.; Aykol, M.; Luo, L.; Wu, J.; Myers, B.D.; Iddir, H.; Russell, J.T.; Saldaña, S.J.; et al. Suppressing Manganese Dissolution from Lithium Manganese Oxide Spinel Cathodes with Single-Layer Graphene. *Adv. Energy Mater.* **2015**, *5*, 1500646. [[CrossRef](#)]
32. Wang, T.; Wang, W.; Zhu, D.; Huang, L.W.; Chen, Y.G. Improvement of the overall performances of  $\text{LiMn}_2\text{O}_4$  via surface-modification by polypyrrole. *Mater. Res. Bull.* **2015**, *71*, 91–97. [[CrossRef](#)]
33. Shi, T.; Dong, Y.; Wang, C.; Tao, F.; Chen, L. Enhanced cycle stability at high rate and excellent high-rate capability of  $\text{La}_{0.7}\text{Sr}_{0.3}\text{Mn}_{0.7}\text{Co}_{0.3}\text{O}_3$ -coated  $\text{LiMn}_2\text{O}_4$ . *J. Power Sources* **2015**, *273*, 959–965. [[CrossRef](#)]
34. Zhang, X.; Xu, Y.; Zhang, H.; Zhao, C.; Qian, X. Structure and cycle stability of  $\text{SrHPO}_4$ -coated  $\text{LiMn}_2\text{O}_4$  cathode materials for lithium-ion batteries. *Electrochim. Acta* **2014**, *145*, 201–208. [[CrossRef](#)]
35. Su, L.; Smith, P.M.; Anand, P.; Jayan, B.R. Surface Engineering of a  $\text{LiMn}_2\text{O}_4$  Electrode Using Nanoscale Polymer Thin Films via Chemical Vapor Deposition Polymerization. *ACS Appl. Mater. Interfaces* **2018**, *10*, 27063–27073. [[CrossRef](#)]
36. Mattelaer, F.; Vereecken, P.M.; Dendooven, J.; Detavernier, C. The influence of ultrathin amorphous ALD alumina and Titania on the rate capability of anatase  $\text{TiO}_2$  and  $\text{LiMn}_2\text{O}_4$  Lithium ion battery electrodes. *Adv. Mater. Interfaces* **2017**, *4*, 1601237. [[CrossRef](#)]
37. Chae, Y.; Lee, J.K.; Choi, W. Surface coating of spinel  $\text{LiMn}_2\text{O}_4$  cathode electrode with lithium–nickel–manganese-oxide by RF sputtering method for lithium-ion batteries. *J. Electroanal. Chem.* **2014**, *730*, 20–25. [[CrossRef](#)]
38. Tang, D.; Yi, R.; Gordin, M.L.; Melnyk, M.; Dai, F.; Chen, S.; Song, J.; Wang, D. Titanium nitride coating to enhance the performance of silicon nanoparticles as a lithium-ion battery anode. *J. Mater. Chem. A* **2014**, *2*, 10375–10378. [[CrossRef](#)]
39. Qiu, Y.; Yan, K.; Yang, S.; Jin, L.; Deng, H.; Li, W. Synthesis of Size-Tunable Anatase  $\text{TiO}_2$  Nanospindles and Their Assembly into Anatase@Titanium Oxynitride/Titanium Nitride–Graphene Nanocomposites for Rechargeable Lithium Ion Batteries with High Cycling Performance. *ACS Nano* **2010**, *4*, 6515–6526. [[CrossRef](#)]

40. Han, H.; Song, T.; Bae, J.Y.; Nazar, L.F.; Kim, H.; Paik, U. Nitridated TiO<sub>2</sub> hollow nanofibers as an anode material for high power lithium ion batteries. *Energy Environ. Sci.* **2011**, *4*, 4532–4536. [[CrossRef](#)]
41. Gao, Y.; Park, J.; Liang, X. Synergic Titanium Nitride Coating and Titanium Doping by Atomic Layer Deposition for Stable- and High-Performance Li-Ion Battery. *J. Electrochem. Soc.* **2018**, *165*, A3871–A3877. [[CrossRef](#)]
42. Li, G.R.; Wang, F.; Jiang, Q.W.; Gao, X.P.; Shen, P.W. Carbon Nanotubes with Titanium Nitride as a Low-Cost Counter-Electrode Material for Dye-Sensitized Solar Cells. *Angew. Chem. Int. Ed.* **2010**, *49*, 3653–3656. [[CrossRef](#)]
43. Milosev, I.; Strehblow, H.H.; Navinsek, B.; Metikoshekovic, M. Electrochemical and thermal oxidation of TiN coatings studied by XPS. *Surf. Interface Anal.* **1995**, *23*, 529–539. [[CrossRef](#)]
44. Avasarala, B.; Haldar, P. Electrochemical oxidation behavior of titanium nitride based electrocatalysts under PEM fuel cell conditions. *Electrochim. Acta* **2010**, *55*, 9024–9034. [[CrossRef](#)]
45. Patsalas, P.; Logothetidis, S. Optical, electronic, and transport properties of nanocrystalline titanium nitride thin films. *J. Appl. Phys.* **2001**, *90*, 4725–4734. [[CrossRef](#)]
46. Angelopoulou, P.; Avgouropoulos, G. Effect of electrode loading on the electrochemical performance of LiAl<sub>0.1</sub>Mn<sub>1.9</sub>O<sub>4</sub> cathode for lithium-ion batteries. *Mater. Res. Bull.* **2019**, *119*, 110562. [[CrossRef](#)]
47. Patsalas, P.; Charitidis, C.; Logothetidis, S. The effect of substrate temperature and biasing on the mechanical properties and structure of sputtered titanium nitride thin films. *Surf. Coat. Technol.* **2000**, *125*, 335–340. [[CrossRef](#)]
48. Patsalas, P.; Logothetidis, S. Interface properties and structural evolution of TiN/Si and TiN/GaN heterostructures. *J. Appl. Phys.* **2003**, *93*, 989–998. [[CrossRef](#)]
49. Patsalas, P.; Logothetidis, S. In-situ monitoring of the electronic properties and growth evolution of TiN films. *Surf. Coat. Technol.* **2004**, *180–181*, 421–424. [[CrossRef](#)]
50. Patsalas, P.; Gravalidis, C.; Logothetidis, S. Surface kinetics and subplantation phenomena affecting the texture, morphology, stress, and growth evolution of titanium nitride films. *J. Appl. Phys.* **2004**, *96*, 6234–6246. [[CrossRef](#)]
51. Patsalas, P.; Kalfagiannis, N.; Kassavetis, S. Optical properties and plasmonic performance of titanium nitride. *Materials* **2015**, *8*, 3128–3154. [[CrossRef](#)]
52. Patsalas, P.; Kalfagiannis, N.; Kassavetis, S.; Abadias, G.; Bellas, D.V.; Lekka, C.; Lidorikis, E. Conductive nitrides: Growth principles, optical and electronic properties, and their perspectives in photonics and plasmonics. *Mater. Sci. Eng. R Rep.* **2018**, *123*, 1–55. [[CrossRef](#)]
53. Logothetidis, S.; Stergioudis, G.; Patsalas, P. Oxidation and structural changes in fcc TiN<sub>x</sub> thin films studied with X-ray reflectometry. *Surf. Coat. Technol.* **1998**, *100–101*, 295–299. [[CrossRef](#)]
54. Jaeger, D.; Patscheider, J. A complete and self-consistent evaluation of XPS spectra of TiN. *J. Elect. Spectrosc. Related Phen.* **2012**, *185*, 523–534. [[CrossRef](#)]
55. Haasch, R.T.; Lee, T.-Y.; Gall, D.; Greene, J.E.; Petrov, I. Epitaxial TiN (001) grown and analyzed in situ by XPS and UPS. II. Analysis of Ar<sup>+</sup> sputter etched layers. *Surf. Sci. Spec.* **2000**, *7*, 204–212. [[CrossRef](#)]
56. Bender, H.; Chen, W.; Portillo, J.; Van den Hove, L.; Wandervorst, W. AES and XPS analysis of the interaction of Ti with Si and SiO<sub>2</sub> during RTA. *Appl. Surf. Sci.* **1989**, *38*, 37–47. [[CrossRef](#)]
57. Pliatsikas, N.; Siozios, A.; Kassavetis, S.; Vourlias, G.; Patsalas, P. Optical properties of nanostructured Al-rich Al<sub>1-x</sub>Ti<sub>x</sub>N films. *Surf. Coat. Technol.* **2014**, *257*, 63–69. [[CrossRef](#)]
58. Bertoti, I.; Mohai, M.; Sullivan, J.L.; Saied, S.O. Surface characterisation of plasma-nitrided titanium: An XPS study. *Appl. Surf. Sci.* **1995**, *84*, 357–371. [[CrossRef](#)]
59. Wolf, M.; Schultze, J.W.; Strehblow, H.-H. Low-energy implantation and sputtering of TiO<sub>2</sub> by nitrogen and argon and the electrochemical reoxidation. *Surf. Interf. Anal.* **1991**, *17*, 726–736. [[CrossRef](#)]
60. Zhu, L.; Lu, Q.; Lv, L.; Wang, Y.; Hu, Y.; Deng, Z.; Lou, Z.; Hou, Y.; Teng, F. Ligand-free rutile and anatase TiO<sub>2</sub> nanocrystals as electron extraction layers for high performance inverted polymer solar cells. *RSC Adv.* **2017**, *7*, 20084–20092. [[CrossRef](#)]
61. Brivio, C.; Musolino, V.; Alet, P.-J.; Merlo, M.; Hutter, A.; Ballif, C. Application-independent protocol for predicting the efficiency of lithium-ion battery cells in operations. *J. Energy Storage* **2018**, *15*, 415–422. [[CrossRef](#)]
62. Winter, M.; Besenhard, J.O.; Spahr, M.E.; Novák, P. Insertion electrode materials for rechargeable lithium batteries. *Adv. Mater.* **1998**, *10*, 725–763. [[CrossRef](#)]
63. Yi, T.F.; Xie, Y.; Wu, Q.J.; Liu, H.P.; Jiang, L.J.; Ye, M.F.; Zhu, R.S. High rate cycling performance of lanthanum-modified Li<sub>4</sub>Ti<sub>5</sub>O<sub>12</sub> anode materials for lithium-ion batteries. *J. Power Sources* **2012**, *214*, 220–226. [[CrossRef](#)]
64. Militello, M.C.; Gaarenstroom, S.W. Lithium Manganese Oxide (LiMn<sub>2</sub>O<sub>4</sub>) by XPS. *Surf. Sci. Spec.* **2001**, *8*, 207–213. [[CrossRef](#)]
65. Militello, M.C.; Gaarenstroom, S.W. Manganese Dioxide (MnO<sub>2</sub>) by XPS. *Surf. Sci. Spec.* **2001**, *8*, 200–206. [[CrossRef](#)]
66. Biesinger, M.C.; Payne, B.P.; Grosvenor, A.P.; Lau, L.W.M.; Gerson, A.R.; Smart, R.S.C. Resolving surface chemical states in XPS analysis of first row transition metals, oxides and hydroxides: Cr, Mn, Fe, Co and Ni. *Appl. Surf. Sci.* **2011**, *257*, 2717–2730. [[CrossRef](#)]